

# Surfactant-Stripped Pheophytin Micelles for Multimodal Tumor Imaging and Photodynamic Therapy

Dana Moukheiber,<sup>†</sup> Upendra Chitgupi,<sup>†</sup> Kevin A. Carter,<sup>†</sup> Dandan Luo,<sup>†</sup> Boyang Sun,<sup>†</sup> Shreya Goel,<sup>‡</sup> Carolina A. Ferreira,<sup>‡</sup> Jonathan W. Engle,<sup>‡</sup> Depeng Wang,<sup>†</sup> Jumin Geng,<sup>†</sup> Yumiao Zhang,<sup>†</sup> Jun Xia,<sup>†</sup> Weibo Cai,<sup>‡</sup> and Jonathan F. Lovell<sup>\*,†</sup>

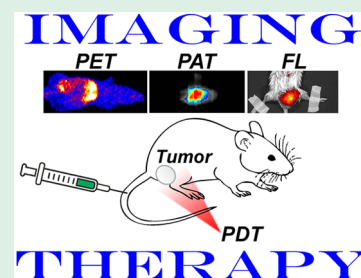
<sup>†</sup>Department of Biomedical Engineering, University at Buffalo, State University of New York, Buffalo, New York 14260, United States

<sup>‡</sup>Department of Radiology, University of Wisconsin-Madison, Madison, Wisconsin 53705, United States

## S Supporting Information

**ABSTRACT:** Porphyrin-based nanomaterials can inherently integrate multiple contrast imaging functionalities with phototherapeutic capabilities. We dispersed pheophytin (Pheo) into Pluronic F127 and carried out low-temperature surfactant-stripping to remove the bulk surfactant. Surfactant-stripped Pheo (ss-Pheo) micelles exhibited a similar size, but higher near-infrared fluorescence, compared to two other nanomaterials also with high porphyrin density (surfactant-stripped chlorophyll micelles and porphysomes). Singlet oxygen generation, which was higher for ss-Pheo, enabled photodynamic therapy (PDT). ss-Pheo provided contrast for photoacoustic and fluorescence imaging, and following seamless labeling with <sup>64</sup>Cu, was used for positron emission tomography. ss-Pheo had a long blood circulation and favorable accumulation in an orthotopic murine mammary tumor model. Trimodal tumor imaging was demonstrated, and PDT resulted in delayed tumor growth.

**KEYWORDS:** pheophytin, photodynamic therapy, micelles, photoacoustic, fluorescence, positron emission tomography



## INTRODUCTION

Photodynamic therapy (PDT) is a clinical ablative modality for treating disease, including cancer, that is based on photosensitizer interaction with targeted delivery of light.<sup>1–3</sup> Photosensitizer irradiation induces generation of singlet oxygen and reactive oxygen species to induce an acute stress reaction leading cellular apoptosis and necrosis.<sup>4</sup> Since photosensitizers passively accumulate in tumors, and because they typically possess inherent fluorescence, they are used for a wide range of tumor optical imaging applications.<sup>5,6</sup> For example, fluorescence imaging of brain tumors has been carried out using Photofrin as a photosensitizer for PDT in brain tumor patients.<sup>7</sup> In addition to localizing tumor sites, photosensitizer fluorescence imaging can be used for PDT dosimetry.<sup>8</sup> Beyond fluorescence imaging, small molecule photosensitizers can be modified with imaging moieties with an additional potential for nuclear or magnetic resonance imaging.<sup>9–11</sup>

Nanomaterials are well-suited to integrate numerous imaging and therapeutic agents into single particles.<sup>12–14</sup> Photosensitizers can be loaded into nanoparticles.<sup>15</sup> A broad variety of nanomaterials have been explored for concurrent imaging and phototherapy, based on diverse compounds including, for example, carbon dots,<sup>16</sup> lanthanides,<sup>17–21</sup> graphene oxide,<sup>22,23</sup> gold,<sup>24,25</sup> iron oxide,<sup>26</sup> silica,<sup>27</sup> micelles,<sup>28</sup> calcium fluoride,<sup>29</sup> albumin,<sup>30</sup> semiconducting polymers,<sup>31–35</sup> and bismuth and tungsten nanoparticles.<sup>36,37</sup> Several other

nanoparticles have been developed with promising photosensitizing capabilities, including some based on semiconducting polymers and BODIPY derivatives.<sup>38–41</sup> Other approaches have been used to optimize phototherapy and multimodal imaging, including biodegradable and pH-sensitive chelated iron nanoparticles and ultrasmall magnetic ternary nanoparticles.<sup>42–44</sup> A wide variety of imaging modalities have been used to image photosensitizers beyond fluorescence optical imaging. Photoacoustic imaging (PAI) is a hybrid optical ultrasonic imaging technique that can image photosensitizers at substantially greater depths than fluorescence optical imaging.<sup>45,46</sup>

Most photosensitizers used in clinical studies are related to the porphyrins, which have an innate theranostic character.<sup>47–49</sup> Numerous nanoparticulate formulations of porphyrins have been developed.<sup>50</sup> Porphyrin-phospholipid conjugates have been demonstrated to self-assemble into nanoscale vesicles known as porphysomes with a highly dense porphyrin bilayer with promise for imaging and phototherapy.<sup>51,52</sup> Another approach toward a high-density porphyrin nanoparticle is to dissolve hydrophobic porphyrins into a surfactant with a temperature-sensitive critical micelle concentration (CMC) and then strip away all free and loose surfactant at low

**Received:** November 12, 2018

**Accepted:** December 19, 2018

**Published:** December 19, 2018

temperatures, leaving behind concentrated, surfactant-stripped (ss) micelles.<sup>53,54</sup> The surfactant-stripping approach has the advantages of minimizing the solubilizing excipient (which could reduce surfactant-related side effects), as well providing an extremely high concentration of cargo. Demetallated chlorophyll (Chlr), pheophytin (Pheo), is highly hydrophobic and has been examined in surfactant-stripped micelle form for intestine imaging.<sup>55</sup> Here, we examine surfactant-stripped Pheo (ss-Pheo) as a unique nanoparticulate agent capable of multimodal contrast imaging and photodynamic therapy.

## ■ EXPERIMENTAL SECTION

**Generation of Pheophytin.** Chlorophyll-a was extracted from chlorella (10 g) by first stirring the biomass in 300 mL of 90% ethanol for 3 h. The solution was then centrifuged at 3400 rpm, and the supernatant was filtered. Then, 48 mL of dioxane was added to 300 mL of chlorophyll-a containing ethanol. A total of 48 mL of water was added to 348 mL of the solution. The solution was kept at  $-20^{\circ}\text{C}$  overnight. The precipitate was then filtered and washed with water. Chlorophyll-a was dissolved in 10 mL of 1 N HCl and 100 mL of ethanol, and then the mixture was stirred for 3 h to remove  $\text{Mg}^{2+}$  from the chlorophyll-a macrocycle. Pheophytin (Pheo) was precipitated by storing it at  $-20^{\circ}\text{C}$  for 3 h; then it was centrifuged, collected, and dried in a desiccator.

**Preparation of Surfactant-Stripped (ss) Micelles.** To prepare ss-Pheo, 10 mg of Pheo was dissolved in 50 mL of dichloromethane (DCM), and then was added dropwise to a 250 mL solution of 10% (w/v) Pluronic F127, with stirring overnight. For a large batch preparation, the washing procedure was conducted using a membrane (Sartorius Vivaflow, 1501008VS) connected to a peristalsis pump (Masterflex L/S). The tubes and membranes were submerged in ice. The solution was washed with 500 mL of water (5 washes, 100 mL each). Centrifugation was conducted with 100 kDa MWCO centrifugal filters to further concentrate ss-Pheo. The centrifugation speed was 3400g, and the temperature was set to  $1^{\circ}\text{C}$ . To make smaller batches, the sample was centrifuged at a speed of 3000g and at  $1^{\circ}\text{C}$  for 30 min using centrifugal filtration tubes with a 100 kDa MWCO membrane. The solution was then concentrated as required using centrifugal filtration. The loading efficacy of ss-Pheo was 100%, as evidenced by no observable loss of Pheo during any point of the formulation or stripping process. The loading capacity of ss-Pheo, considering the entrapped Pheo divided by the total mass including Pluronic, was 26%.

To prepare ss-Chlr, 10 mg of Chlr was dissolved in 50 DCM, and then added dropwise in 250 mL 10% (w/v) Pluronic F127 with stirring overnight. The surfactant-stripping procedure was conducted in the same manner as ss-Pheo.

To determine the surfactant-stripping efficacy, a small scale washing procedure was conducted to make 10 mL of ss-Pheo. Pheo (0.4 g) was dissolved in 2 mL of DCM, and the mixture was added to 10 mL of 10% F127; then DCM evaporated. ss-Pheo was washed with a low-temperature centrifugal filtration 4 times. After each wash, 1 mL of each filtrate was collected until about 200  $\mu\text{L}$  of the sample was retained in the 100 kDa MWCO centrifugal filters. The sample was then adjusted to 200  $\mu\text{L}$  with water. Then, 0.3 g of cobalt nitrate hexahydrate and 1.2 g of ammonium thiocyanate were dissolved in 3 mL of water to make cobalt thiocyanate. To measure the absorbance of F127 at 623 nm in the sample and filtrate, 200  $\mu\text{L}$  of ethyl acetate, 80  $\mu\text{L}$  of ethanol, and 100  $\mu\text{L}$  of cobalt thiocyanate solution were added to 200  $\mu\text{L}$  of filtrate and sample. The solution was vortexed for 10 s and centrifuged for 5 min at 10 000 rcf in 1.5 mL centrifuge tubes. The solution was washed with ethyl acetate, and the supernatant was removed about 3 times or more as needed until the supernatant was colorless. One mL of acetone was added to dissolve the blue pellet. Absorbance was then measured using Lambda 35 UV-vis or a Lambda XLS spectrophotometer (PerkinElmer). The absorbance of F127 in the retentates and filtrates was measured at 623

nm. The absorbance of the dye in the retentates and filtrates was measured at 670 nm for quantification.

**Preparation of Porphyosomes.** Lipids were dissolved in ethanol to form a stock solution with the following formulation, [Pyrophospholipid/PEG/cholesterol] with a molar ratio of [5:5:40]. At  $60^{\circ}\text{C}$ , 800  $\mu\text{L}$  of phosphate buffered saline (PBS) was added to 200  $\mu\text{L}$  of ethanol. The liposome solution was extruded 20 times through a hand-held extruder. Gel filtration chromatography was used to collect the liposomal fractions.

**Nanoparticle Characterization.** Absorbance was measured with a Lambda 35 UV-Vis or a Lambda XLS spectrophotometer (PerkinElmer) using cuvettes with a 1 cm path length. The particle size and polydispersity index for each sample were obtained by dynamic light scattering in phosphate buffered saline (PBS). These measurements were determined by a Nano ZS 90 Zetasizer (Malvern Instruments). Transmission electron microscopy was performed using a JEM-2010 electron microscope with 1% uranyl acetate for negative staining.

For fluorescence emission spectra, the absorbance of each sample was adjusted to 0.05, and the emission spectra was recorded at 410 nm excitation wavelength using a Photon Technology International (PTI) fluorimeter. The relative quantum yield was calculated by integrating the area under the curve for the fluorescence spectra between 650 and 800 nm. For ss-Pheo, ss-Pheo was dissolved in  $\text{CHCl}_3$  and ss-Pheo was mixed with 0.1% Triton X-100, respectively. The excitation wavelength was set at 410 nm, and the emission was scanned in range from 500 to 800 nm.

For singlet oxygen determination, Singlet Oxygen Sensor Green (SOSG; Life Technologies no. S-36002) was used to determine singlet oxygen production following light irradiation, and 0.6  $\mu\text{M}$  SOSG was used. The samples were normalized at an absorbance of 0.5 at 665 nm, and 2  $\mu\text{L}$  of SOSG stock solution was added to 3 mL of each sample. The solution was irradiated for 5 min in a 3 mL cuvette with stirring.

For the absolute quantum yield, an equal absorbance based on UV-vis spectra was used at the excitation wavelength in a fluorescence emission scan in a PTI instrument. The buffer background was subtracted from each fluorescence reading obtained from the emission scan. The area under the curve (AUC) was determined. The quantum yield of Pheo in methanol was used as a standard. The quantum yield for the sample was multiplied by the AUC of the sample in water divided by the AUC of the sample in methanol to obtain the quantum yield of Pheo in water.

**Comparison of Surfactant-Stripping to Other Pheo Formulations.** For ethanol dilution and solvent exchange formulations, 15 mg/mL Pheo in ethanol (close to its maximum solubility) was added to 10% (w/v) surfactant solutions including Tween 80, Cremophor EL, Pluronic F127, or Pluronic F68 so that the ethanol formed 20% of the final volume. The solutions were then placed in dialysis tubing and dialyzed against 0.5 L of PBS. The buffer was changed two times after dialysis proceeded for at least 4 h. For solvent evaporation formulations, 30 mg/mL Pheo in DCM was prepared. Pheo (100  $\mu\text{L}$ ) solution was added dropwise to 1 mL of 10% w/v surfactant solutions. The solutions were left to stir and evaporate overnight. For liposomal Pheo formulations, dry lipid powders (94.1 mg of DPPC and 5.9 mg of Pheo) were mixed in 5 mL of PBS solution and then were sonicated at  $60^{\circ}\text{C}$  for 1 h. Concentrated liposomes were prepared by freeze-drying the liposomes and resuspending in just 60% of the original volume. Aggregated liposomes were removed by centrifugation. The absorbance of the solutions was assessed with a UV-vis spectrometer at 665 nm.

**Photothermal and Photostability Properties.** Different concentrations of ss-Pheo from 0 to 2 mg/mL were used. A 665 nm laser was used to irradiate the samples. Thermal imaging was conducted to monitor the temperature increase over 3 min. Photobleaching of 1  $\mu\text{g}/\text{mL}$  ss-Pheo was tested in water under various 665 nm laser fluence rates from 0 to 300  $\text{mW}/\text{cm}^2$  for 5 min. An emission scan was then obtained using a PTI fluorometer with an excitation wavelength of 410 nm.

**Hemolysis.** Blood was obtained in citrate solution from adult human volunteers following informed consent. Protocols were approved by the University at Buffalo Health Science Institutional Review Board. The erythrocyte suspension was prepared by centrifugation at 420g for 10 min. Isotonic PBS was added to the suspension, and it was further centrifuged at 3000g for 10 min. The supernatant was removed, and the washing procedure was repeated to thoroughly remove undamaged erythrocytes. Pheophytin surfactant solutions were prepared by adding 0.2 mg of Pheo (dissolved in 1 mL of DCM) in 5 mL of 10% (w/v) Tween-80 or F127 solutions. Following solvent evaporation, Pheo was diluted with PBS to achieve the desired Pheo concentrations. A total of 5  $\mu\text{L}$  of Pheo was incubated with 15  $\mu\text{L}$  of RBC at 37 °C for 1 h, followed by centrifugation at 2000g for 5 min. The absorbance of supernatant at each concentration was measured using spectrophotometry at the max absorbance wavelength of 540 nm. Hemolysis percentages were determined using an absorbance reading where % hemolysis =  $[\text{sample} - \text{negative}/\text{positive} - \text{negative}] \times 100\%$ . PBS was used as a negative control, and red blood cells with TX-100 were used as a positive control.

**In Vitro Imaging.** Fluorescence imaging was measured using an IVIS Lumina II system. An excitation of 675 nm was used with an ICG emission filter. Samples were normalized at an absorbance of 0.5 at 675 nm. The fluorescence was measured by stacking 1 mm slices of ham over the sample tubes placed 1 cm apart. Fluorescence counts of the three samples were measured using the ROI tool in the IVIS software and background signal was corrected for.

For photoacoustic (PA) imaging, 1.5 mm inner diameter silicon tubes were used. Three pieces of tubes were filled with three different samples, respectively, and then were imaged one by one. Tubes without any chicken breast tissue at the top were first measured. After that, PA imaging was conducted when 11 mm chicken breast tissue was placed on top of tubes. Pieces of chicken breast tissues were supported by the agar phantom (2 cm in thickness) placed at the bottom of tubes.

The excitation light for PA imaging was provided by a Nd:YAG laser, which output was routed to tube phantoms in free space. Using ground glass as a diffuser, the laser beam was uniformly distributed roundly on the phantom surface with a 2 cm diameter. The maximum light intensity at the phantom surface was around 12 mJ/cm<sup>2</sup>, which is far below the American National Standards Institute (ANSI) safety limit (20 mJ/cm<sup>2</sup>). The PA signal of tubes was acquired by a 128-element clinical liner transducer array (ATL/Philips L7-4) with a 5 MHz central frequency. The received PA signals were amplified (by 54 dB) and digitized by a 128-channel ultrasound data acquisition (DAQ) system (Vantage, Verasonics) with a 20 MHz sampling rate. The raw channel data was reconstructed using the universal back-projection algorithm (Xu and Wang 2005) and was displayed in real-time during experiments.<sup>56</sup>

**Cell Culture and PDT.** Murine mammary cancer cells (4T1) were cultured in RPMI-1640 medium supplemented with 10% fetal bovine serum (FBS) and 1% streptomycin/penicillin. Cells were cultured in 25 cm<sup>2</sup> flasks maintained at 37 °C and 5% CO<sub>2</sub>. Photodynamic therapy experiments were performed in a 96-well plate. Cells were seeded at a density of 10<sup>4</sup> cells per well and allowed to adhere for 24 h. ss-Pheo was added to wells containing serum containing media and incubated for 4 h. Media was removed and cells were washed with PBS and fresh media was added. Cells were exposed to a laser using a 665 nm custom-built LED box at various fluences. A constant fluence rate of 29.8 mW/cm<sup>2</sup> was used to irradiate cells. Efficacy of PDT in vitro was evaluated by a cell viability assay. Cells were allowed to grow for 24 h after laser treatment. At this point, media was removed and the cells were washed with PBS to remove traces of media. Then, 100  $\mu\text{L}$  of PBS containing 50  $\mu\text{g mL}^{-1}$  2,3-bis(2-methoxy-4-nitro-5-sulphophenyl)-2H-tetrazolium-5-carboxanilide (XTT) and 30  $\mu\text{g mL}^{-1}$  N-methyl dibenzopyrazine methyl sulfate (PMS) were added to each well and incubated for 2 h. The tetrazolium dye, XTT, is colorless but when reduced to formazan product it becomes brightly orange. The reduction is improved by the addition of the activation reagent PMS. The absorbance of the plate was read at 450 nm, and the absorbance

at 630 nm was used as a background. Cell viability was calculated as a ratio of viability of treated cells to untreated cells. All experiments were carried out in triplicates, and error bars indicated the standard deviation from the mean value.

To test cell death mechanisms, cells were seeded in a 24-well plate with a starting cell density of 50 000 cells per well. Cells were incubated at 37 °C and 5% CO<sub>2</sub> for 24 h. Pheo was added at 0.02 mg mL<sup>-1</sup> in media, and the mixture was incubated for 4 h. After the incubation period was complete, the medium containing micelles was removed and the cells were washed with PBS twice. Then, fresh medium containing FBS was added. Cells were treated with a 665 nm laser for 9 min at 18.67 mW cm<sup>-2</sup> to deliver a fluence of 10 J/cm<sup>2</sup>. After laser treatment, cells were placed in the incubator for 24 h and samples were analyzed using flow cytometry. The medium was removed, and the cells were incubated with 0.5 mL of trypsin for 4 min. After the cells were cleaved, 0.7 mL of medium containing FBS was added. Cells were collected in individual vials and were centrifuged at 500 rpm for 5 min. Supernatant was removed, and 0.5 mL of 0.1% bovine serum albumin was added. Samples were centrifuged at 500 rcf for 5 min, and 0.4 mL of supernatant was removed. Cells were treated with the Biologend Annexin-PI kit according to the manufacturer's recommendations. Flow cytometry was carried out using a BDFortessa instrument. Samples were vortexed immediately before analysis. Data was analyzed using FloJo software.

**Pharmacokinetics and Biodistribution.** Animal experiments were carried out in compliance with the Institutional Care and Use Committee guidelines at the University at Buffalo. Female BALB/c mice (18–20 g) were used, and 200  $\mu\text{L}$  containing 25 “optical density” (OD) ss-Pheo samples were injected via the tail vein. One OD represents an absorbance at 670 nm of ss-Pheo if dissolved in a 1 mL solution and measured in a 1 cm path length cuvette. Twenty-five OD corresponds to approximately 500  $\mu\text{g}$  of ss-Pheo. Blood samples were collected at different time intervals. The collection time points that were used were 0.5, 1, 2, 4, 8, 24, and 48 h. The samples were then centrifuged at 2000g for 15 min. After that, 10  $\mu\text{L}$  of serum was added to 990  $\mu\text{L}$  of extraction buffer. Then it was vortexed and kept in cold storage at -20 °C for at least 2 h. The solution was then centrifuged at 10 000g for 15 min. Then, 200  $\mu\text{L}$  of supernatant was used to read the fluorescence. A standard curve was used to quantify the drug amount. Noncompartmental analysis with PK solver was used to determine the half-life of ss-Pheo.

For tumor biodistribution studies,  $2 \times 10^4$  4T1 cells in 50  $\mu\text{L}$  of RPMI 1640 medium (without serum) were injected subcutaneously at the base of the nipple into the fourth abdominal fat pad of 4–8 week old female BALB/mice. Tumor growth was measured over time using digital calipers. Mice were treated when the tumor size reached 6–8 mm. Then, 200  $\mu\text{L}$  containing 25 OD at 670 nm of ss-Pheo (500  $\mu\text{g}$ ) was injected via the tail vein of BALB/c mice bearing orthotopic 4T1 tumors. BALB/c mice with no tumors were used as a control. Organs and tissue (about 100 mg) were weighed, and 450  $\mu\text{L}$  of nuclear lysis buffer [0.25 mol/L sucrose, 5 mmol/L Tris-HCl, 1 mmol/L MgSO<sub>4</sub>, 1 mmol/L CaCl<sub>2</sub> (pH 7.6)] was added to the tissue ready for desiccation in a Bullet Blender homogenizer. Ss-Pheo was extracted using 0.075 N HCL 90% isopropanol and left overnight. After centrifugation the next day, the supernatant was diluted using extraction buffer and measured using a fluorescence plate reader. Concentrations were determined from a standard curve obtained from ss-Pheo in extraction buffer.

**<sup>64</sup>Cu Radiolabeling.** Copper-64 (<sup>64</sup>Cu,  $t_{1/2} = 12.7$  h) was produced in an on-site cyclotron (GE PETrace) at the University of Wisconsin-Madison, via <sup>64</sup>Ni (p,n) <sup>64</sup>Cu reaction as reported earlier. For radiolabeling, 37 MBq of <sup>64</sup>CuCl<sub>2</sub> was diluted in 300  $\mu\text{L}$  of 0.1 M sodium acetate buffer, (pH ~ 5.5) and added to 300 OD ss-Pheo. The mixture was incubated at 37 °C for 60 min with constant shaking, followed by purification on an Amicon Ultra-4 centrifugal filter unit (Millipore) using PBS. Final radiolabeling yields were determined with thin-layer chromatography (TLC), using silica gel-backed iTLC plates, with 50 mM EDTA solution as the running buffer.

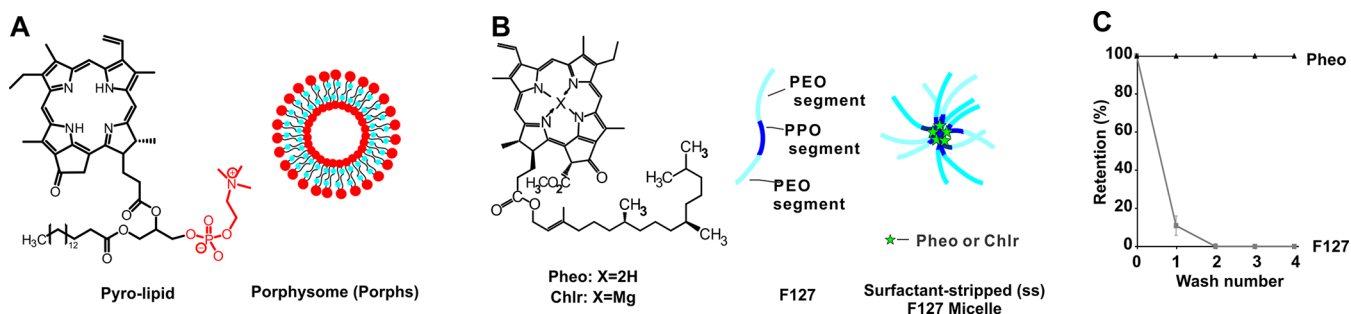


**Figure 1.** Structure and representation of high-density porphyrin nanoparticles. (A) Pyro-lipid self-assembles to form porphysome nanovesicles with a porphyrin bilayer. (B) Chlorophyll (Chlr) or pheophytin (Pheo) can be formed into surfactant-stripped micelles with Pluronic F127 triblock copolymers. (C) Retention of Pheo and F127 during the surfactant-stripping process to generate ss-Pheo. Data show mean  $\pm$  standard deviation for  $n = 3$ .

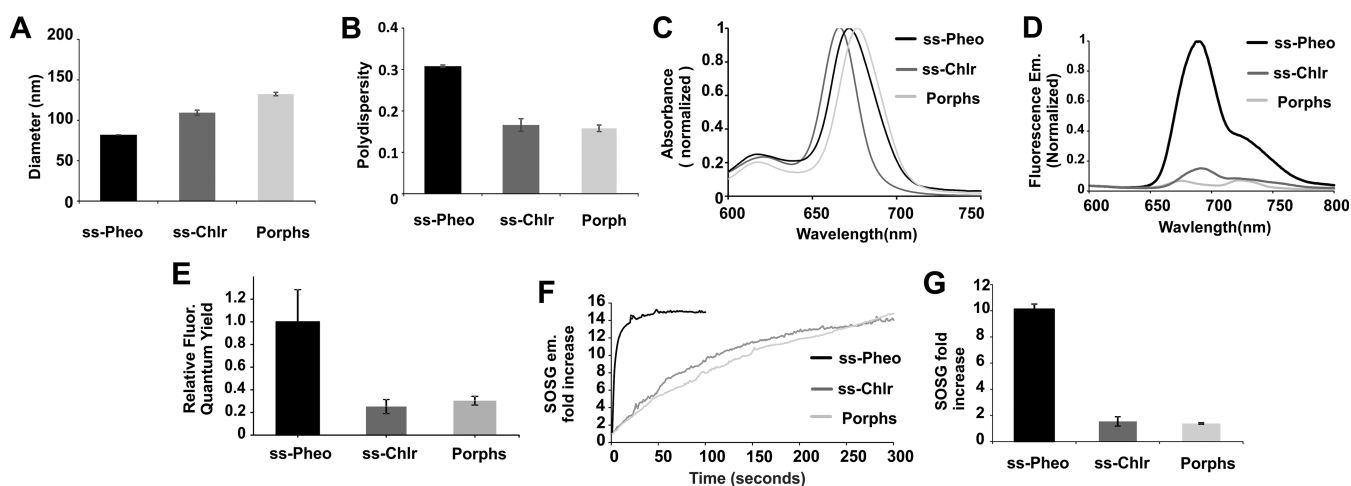


**Figure 2.** Characterization of porphyrin nanomaterials. (A) Hydrodynamic diameter and (B) polydispersity index of ss-Pheo, ss-Chlr, and Porphs as determined by dynamic light scattering. (C) Q-band normalized absorption spectra in water. (D) Fluorescence emission spectra when nanoparticles were adjusted to have an absorbance of 0.05 at the excitation wavelength. Spectra are normalized to ss-Pheo emission maximum. (E) Relative fluorescence quantum yield. (F) Singlet Oxygen Sensor Green (SOSG) indicator dye signal increases as ss-Pheo, ss-Chlr, or porphysomes were irradiated at 665 nm (when adjusted to have an equal absorbance at 665 of 0.05). (G) Initial rate of SOSG increase during the first 5 s of irradiation. Values show mean  $\pm$  standard deviation for  $n = 3$ .

For radiolabeling, 18.5 MBq of  $^{64}\text{CuCl}_2$  was diluted in 300  $\mu\text{L}$  of 0.1 M sodium acetate buffer, (pH of 5.5) and added to 150  $\mu\text{L}$  of 25 OD ss-Pheo. The mixture was incubated at 37  $^\circ\text{C}$  for 60 min with constant shaking, followed by the purification by an Amicon Ultra-4 centrifugal filter unit (Millipore) using PBS. To assess the serum stability of  $^{64}\text{Cu}$  radiolabeled Pheo ss-InFroMs, ss-InFroMs was incubated with fetal bovine serum 60% (400  $\mu\text{L}$  of nanoparticles in PBS added to 600  $\mu\text{L}$  of FBS) at 37  $^\circ\text{C}$  with constant agitation (500 rpm). At different time points, as shown in the figure, 100  $\mu\text{L}$  aliquots were taken and centrifuged using the Centriscart ultrafiltration (300 000 MWCO) system, and the radioactivity in the filtrate and retentate were measured using a  $\gamma$  counter and decayed back to day 0 for further calculations.

**PET Imaging.** For PET imaging, animal studies were carried out in accordance with the University of Wisconsin-Madison Institutional Animal Care and Use Committee. For tumor PET imaging studies,  $1 \times 10^6$  4T1 murine breast cancer cells suspended in 30  $\mu\text{L}$  of PBS were injected in the fourth mammary pad of 5–6 week old female BALB/c mice (Envigo, IN). Tumor sizes were monitored regularly, and mice were used when the tumors reached  $\sim 7$  mm in diameter, typically 7–10 days post-inoculation. Twenty-five OD of  $^{64}\text{Cu}$ -labeled Pheo nanoparticles was injected intravenously in 4T1 tumor-bearing mice via the tail vein ( $n = 3$ ). Static positron emission tomography (PET) images were acquired at different time points postinjection (p.i.) on an Inveon microPET/microCT rodent model scanner (Siemens Medical Solutions USA, Inc.). All PET images were reconstructed

using a maximum a posteriori algorithm, without attenuation or scatter correction, and analyzed with Inveon Research Workplace software after decay correction. All data are presented as a percentage injected dose per gram (%ID/g). Mice were euthanized after the final PET scans at 72 h postinjection, and ex vivo biodistribution studies were performed, to validate the in vivo results. Blood, tumor, and major organs were collected and wet-weighted, and radioactivity in each tissue was measured on a WIZARD $^2$   $\gamma$  counter (PerkinElmer) and presented as %ID/g.

**In Vivo Optical Imaging.** Fluorescence imaging was conducted 24 h after injection of 200  $\mu\text{L}$  of 25 OD ss-Pheo in the mice (500  $\mu\text{g}$  ss-Pheo). Mice were anesthetized using isoflurane. Fluorescence was then measured at 640 nm excitation and Cy 5.5 emission for the control and treated mice using an IVIS imaging system. PAT scans were conducted 24 h after injection of 200  $\mu\text{L}$  of 25 OD ss-Pheo (500  $\mu\text{g}$ ) in the mice. During experiments, tumor-bearing mice were placed underneath a water tank with a window at the bottom. A 690 nm pulse laser light was provided by a Nd:YAG pumped optical parametric oscillator (OPO) laser (SLIII-10, Continuum) with a 10 Hz pulse repetition rate and 10 ns pulse duration. The light was routed to the tumor surface through a bifurcated fiber bundle with one circular input and two linear outputs ( $\sim 60\%$  coupling efficiency). The light intensity on the tumor surface was around 13  $\text{mJ}/\text{cm}^2$ , which is below the American National Standards Institute (ANSI) safety limitation at 690 nm (20  $\text{mJ}/\text{cm}^2$ ). The PA signal of tumor was acquired by a 128-element clinical liner transducer array (ATL/

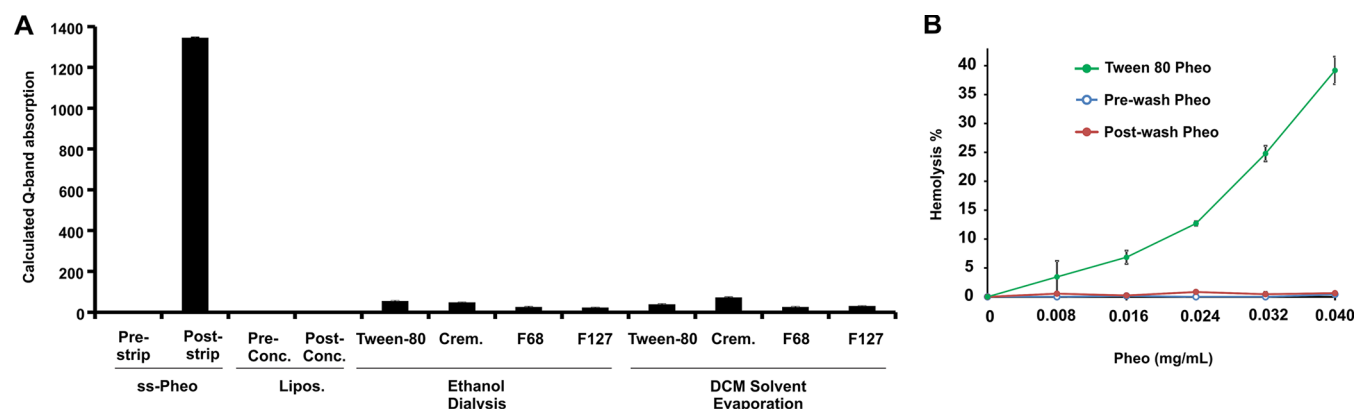


**Figure 3.** Surfactant-stripping enables concentrated micelle dispersions. (A) Absorbance of concentrated ss-Pheo compared to conventional formulation methods. (B) Hemolysis of Pheo samples at indicated concentrations following incubation with human red blood cells for 1 h at 37 °C. Values show mean  $\pm$  standard deviation for  $n = 3$ .

Philips L7-4) with a 5 MHz central frequency. The transducer was scanned over a 4 cm distance with a 0.1 mm step size image of the whole tumor. The received PA signals were amplified (by 54 dB) and digitized by a 128-channel ultrasound data acquisition (DAQ) system (Vantage, Verasonics) with a 20 MHz sampling rate. The raw channel data was reconstructed using the universal back-projection algorithm and was displayed in real-time during experiments.

**PDT Efficacy Study.** Four week old mice were procured from the Charles River laboratory. Animal experiments were performed in accordance with the University at Buffalo Institutional Animal Care and Use Committee. 4T1 cells ( $2 \times 10^4$ ) were subcutaneously injected into mice. Mice were randomly divided into four groups with 5 mice in each group. When the tumor size reached 5–7 mm, mice were intravenously injected with either ss-Pheo or PBS via the tail vein. Twenty-four h postinjection, two groups (laser alone, ss-Pheo +laser) were treated with a laser. For the laser treatment, mice were anesthetized with isoflurane and tumors were irradiated with a 665 nm laser at  $150 \text{ mW cm}^{-2}$  for 33 min, delivering a total energy of  $300 \text{ J cm}^{-2}$ . The tumor temperature was monitored using a thermal camera. Pheophytin alone and untreated groups did not receive any laser treatment.

## RESULTS AND DISCUSSION

We examined 3 types of high-density porphyrin nanoparticles. Porphysomes (Porphs) were formed from pyro-lipid (sn-1-palmitoyl sn-2-pyropheophorbide phosphatidylcholine) (Figure 1A). Pyro-lipid comprised the major component of the bilayer (55 mol %). We also prepared two types of surfactant-stripped micelles from either chlorophyll (Chlr) or pheophytin (Pheo), using Pluronic F127 to disperse the molecules prior to surfactant-stripping using a low-temperature cross-flow membrane filtration process (Figure 1B). Pheo or Chlr was first dissolved in dichloromethane (DCM) and then added dropwise to a F127 solution, with stirring overnight to incorporate in the hydrophobic poly(propylene oxide) cores of Pluronic F127 micelles. Taking advantage of temperature-sensitive micellization of F127, excess and free F127 were dissociated into F127 unimers at a low temperature (4 °C) and then “stripped” away by membrane filtration, leaving behind purified and concentrated ss-Pheo. As shown in Figure 1C, during the surfactant-stripping process, Pheo was fully retained in ss-micelles, whereas all free and loose F127 were effectively removed, with four low-temperature washing steps, generating a colloidal suspension with a high porphyrin density.

The diameter and polydispersity of the 3 types of nanoparticles (Porphs, ss-Pheo, and ss-Chlr) were measured

(Figure 2A,B). The hydrodynamic size distribution is shown in Figure S1. Overall, the size of the three types of nanoparticles was similar. ss-Pheo had the greatest polydispersity of about 0.3 and the smallest diameter of about 80 nm. Transmission electron microscopy revealed a spherical morphology for ss-Pheo. (Figure S2).

The porphyrin component of all three types of nanoparticles is chlorophyll-derived, and the aqueous absorption spectra were similar between the different formulations, with a Q-band peak around 670 nm (Figure 2C). ss-Chlr, ss-Pheo, and Porphs had Q-band absorption maxima at 665, 672, and 677 nm, respectively.

Although the absorption properties of the different porphyrin nanoparticles were similar, stark contrasts were encountered in the emission properties. ss-Pheo showed the brightest fluorescence emission compared to porphsomes and ss-Chlr, with an emission peak at 690 nm (Figure 2D) and the greatest relative quantum yield (Figure 2E). The mechanism for the higher fluorescence quantum yield of ss-Pheo may potentially relate to a more hydrophobic local environment of pheophytin, as it is more hydrophobic than Chlr, or porphyrin-phospholipid. These results are consistent with the initial report of ss-Pheo, where it was suggested that stacking differences within the micelle may contribute to the enhanced relative brightness.<sup>55</sup> Further work is required to better elucidate the photophysical structure–function properties. Despite the higher fluorescence of ss-Pheo compared to other high-density porphyrin structures, the absolute fluorescence quantum yield was low and was calculated to be just 3% of the yield of Pheo dissolved in methanol, which has been reported as 0.14 (Figure S3).<sup>57</sup>

It is known that the quenched porphyrin fluorescence quantum yield correlates with quenching of the singlet oxygen yield.<sup>58</sup> The reporter dye Singlet Oxygen Sensor Green<sup>59</sup> was used to assess singlet oxygen generation of the nanoparticles in an aqueous solution under irradiation with a 665 nm laser diode. ss-Pheo induced a rapid increase in SOSG signal, indicating the generation of singlet oxygen, whereas ss-Chlr and porphsomes had a substantially slower rate of SOSG activation (Figure 2F). Figure 2G shows the SOSG activation in the initial 5 s of porphyrin nanoparticle irradiation, in which strongly enhanced singlet oxygen generation by ss-Pheo was observed.

One of the unique features of surfactant-stripped micelles is that since the bulk solubilizing surfactant can be removed, the

cargo-loaded micelles can be further concentrated to very high levels. Figure 3A shows that the surfactant-stripped approach can produce concentrated Pheo micelle dispersions with a much higher Q-band (i.e., around 665 nm) absorption compared to conventional formulation techniques for hydrophobic cargo. Those formulations, such as liposomes, or Pheo-ethanol (at a maximum Pheo concentration) mixing followed by dialysis or Pheo-DCM mixing followed by solvent evaporation are not readily concentrated, so the overall absorption was much lower. A high concentration of Pheo may be useful for various applications, such as photoacoustic and photothermal contrast. ss-Pheo showed a photothermal contrast and generated heat in a concentration-dependent fashion upon irradiation with a 665 nm, 0.4 W/cm<sup>2</sup> laser (Figure S4).

As shown in Figure 3B, when Pheo was dissolved in Tween-80 and incubated with human erythrocytes, hemolysis was observed. Interestingly, with the exact same formulation but using Pluronic F127 instead of Tween-08, minimal hemolysis was induced. As expected, after surfactant-stripping, no hemolysis was observed.

Next, optical imaging was carried out in tissue phantoms. For fluorescence imaging, increasing layers of thin ham slices were layered above the porphyrin nanoparticle samples. As shown in Figure 4A, only ss-Pheo was readily detected with

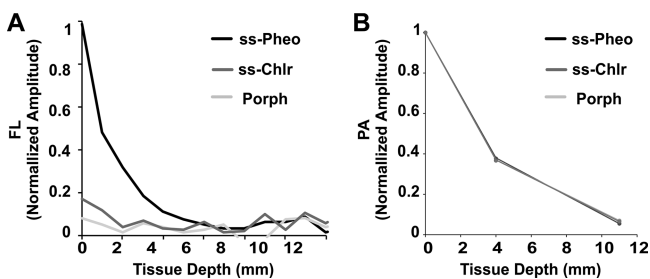


**Figure 4.** In vitro imaging of porphyrin nanoparticles using fluorescence and PAT. (A) Signal intensity in fluorescence counts for three photosensitizers as a function of tissue depth. (B) PAT signal intensity against tissue depth.

fluorescence imaging (to a depth of approximately half a centimeter). Photoacoustic contrast imaging produced different results (Figure 4B). All three types of porphyrin nanomaterials could be detected in tissue to a depth of 1 cm when the samples were adjusted to have an equal NIR absorption of 0.5.

Together, these data show that ss-Pheo has similar physical properties to ss-Chlr and porphyrins as well as a similar optical absorption. However, ss-Pheo exhibits a higher fluorescence and singlet oxygen yield, features which are appealing for PDT and imaging applications. Thus, for all subsequent studies, ss-Pheo was chosen for further investigation.

In vitro PDT was assessed by examining the cell viability with the XTT assay following treatment (Figure 5A). ss-Pheo was incubated with murine mammary 4T1 cancer cells for 4 h, then the medium was replaced, and cells were treated with a 665 nm LED box. With no laser irradiation or with treatment but no laser irradiated, the cell viability was found to be unaffected. With both laser- and ss-Pheo-treated cells, the cell viability of 4T1 cancer cells was found to decrease. When 0.05 mg/mL of ss-Pheo was used, the cell viability started to

decrease due to the PDT effect. When irradiated with 10 J/cm<sup>2</sup> and 20 J/cm<sup>2</sup>, the cell viability was found to be 80% and 35%, respectively. Further work is required to elucidate the mechanism of uptake; however, it is possible that the photosensitizer in ss-Pheo micelles underwent exchange with cell medium components that were uptaken by cells, and/or that ss-Pheo itself was uptaken by cells, and/or that the photosensitizers were able to directly transport to cellular membranes. Thus, ss-Pheo is able to serve as a photosensitizer to kill cancer cells in vitro with 665 nm light application. Cell killing was further assessed through staining of the apoptosis marker Annexin V and the cell permeability marker propidium iodide (PI) (Figure 5B). Unlike control cells or cells incubated with ss-Pheo without laser treatment, cells treated with 0.02 mg/mL ss-Pheo at 10 J/cm<sup>2</sup> fluence were stained by Annexin V and PI. A total of 34% of cells was classified in late apoptosis (Annexin V<sup>+</sup>; PI<sup>+</sup>), 34% of cells were in early apoptosis (Annexin V<sup>+</sup>; PI<sup>-</sup>), and 8% of cells were considered necrotic (Annexin V<sup>-</sup>; PI<sup>+</sup>). This is consistent with the XTT assay data, which shows that Pheo ss-InFroMs + laser-treated cells induce a greater cell death.

To assess the photostability of ss-Pheo, 1 μg/mL was irradiated under 665 nm laser irradiation for 5 min. With increasing fluence rates, photobleaching became more prominent (Figure S5). At the highest fluence rate (300 mW/cm<sup>2</sup>), approximately 30% photobleaching was observed.

Next, we investigated the in vivo behavior of ss-Pheo. Even though ss-Pheo exhibited a strong fluorescence compared to ss-Chlr or porphyrins, it was still self-quenched relative to its brightness in organic solvents. We found that with the addition of the detergent (0.1% Triton X-100, TX100), the fluorescence of ss-Pheo increased to a point similar to dissolving ss-Pheo in organic solvent such as chloroform, so this approach was used for analytical measurements (Figure S6).

Following intravenous administration of ss-Pheo, serum was sampled periodically and the blood concentration was estimated with a fluorometric assay. ss-Pheo had relatively long blood circulation of 14.2 h, as determined by non-compartmental analysis (Figure 6). The relatively long circulation could be in part due to the polyethylene oxide (PEO) blocks of the F127 triblock copolymer, which are known to confer stealth properties to nanoparticles.<sup>60</sup>

The uptake of ss-Pheo was next assessed in mice bearing orthotopic 4T1 tumors, 24 h following intravenous injection. As shown in Figure 7A, Pheo accumulated to a relatively high degree in tumor tissue, based on the fluorescence signal in extracted from homogenized tissues. Most of the Pheo was distributed in the liver. These biodistribution findings were confirmed in a separate independent experiment using <sup>64</sup>Cu-radiolabeled ss-Pheo, with similar distribution patterns with the ss-micelles principally distributed in the liver, tumor, spleen, and then kidney, in a decreasing order (Figure 7B). The chelation stability of the radioisotope in <sup>64</sup>Cu ss-Pheo was tested in fetal bovine serum before administration in living animals showing over 60% of chelated <sup>64</sup>Cu retention in the nanoparticle after 48 h (Figure S7). The strong uptake of ss-Pheo in the liver is typical for many long-circulating intravenously administered nanoparticles, based on uptake by the reticuloendothelial system.<sup>61</sup> On the other hand, accumulation of ss-Pheo in the tumor may be attributed to the enhanced permeability and retention effect in tumor vasculature.

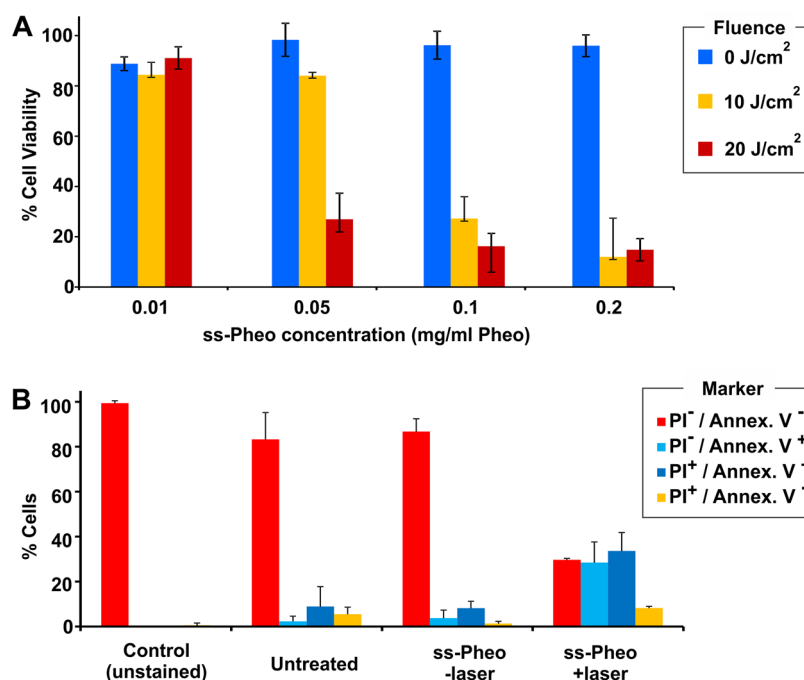


**Figure 5.** Cell death induced by PDT with ss-Pheo. (A) Cells were incubated with ss-Pheo at indicated concentrations for 4 h and then subjected to light treatment with a 665 nm LED box. Cell viability was assessed 24 h after laser treatment using the XTT assay. (B) Following the indicated treatment, 4T1 cells were stained with Annexin V and PI and subjected to flow cytometry. Values show mean  $\pm$  standard deviation for  $n = 3$ .

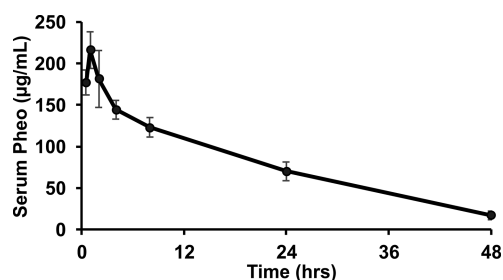


**Figure 6.** Pheo concentration in serum in mice following intravenous administration of ss-Pheo (500  $\mu\text{g}$  Pheo dose). Data shows mean  $\pm$  standard deviation for  $n = 3$  mice.

Trimodal imaging was used to monitor the accumulation of ss-Pheo in the tumor and other organs. In all cases, 0.5 mg of ss-Pheo was injected per mouse. This dose produces a NIR absorption of 25 if dissolved in 1 mL of water and measured with a standard 1 cm path length cuvette.  $^{64}\text{Cu}$  labeling was carried out by simply incubating preformed ss-Pheo with the

radioisotope in aqueous solution, due to the high affinity of copper ions with porphyrins. A 60% labeling yield was observed. Figure 8A shows the PET scan of mice bearing 4T1 tumors. The corresponding %ID/g for each corresponding time for the liver, heart, muscle, and tumor, respectively, calculated on imaging data is shown in Figure S8. A strong signal was present in the liver, and by the later time points, the tumor was clearly visualized. These results are consistent with the biodistribution study, which showed that ss-Pheo was taken up mostly in the liver and tumor (Figure 7). Given the optical properties of ss-Pheo, fluorescence imaging was intrinsically possible, something that is not always possible for photoacoustic materials, as a high chromophore density that is desirable for photoacoustic contrast can lead to fluorescence self-quenching. Figure 8B,C shows the fluorescence imaging and photoacoustic imaging of mice using ss-Pheo as a contrast agent with the control left untreated. Unlike PET imaging, which is a whole-body imaging modality, fluorescence and photoacoustic imaging only revealed the ss-

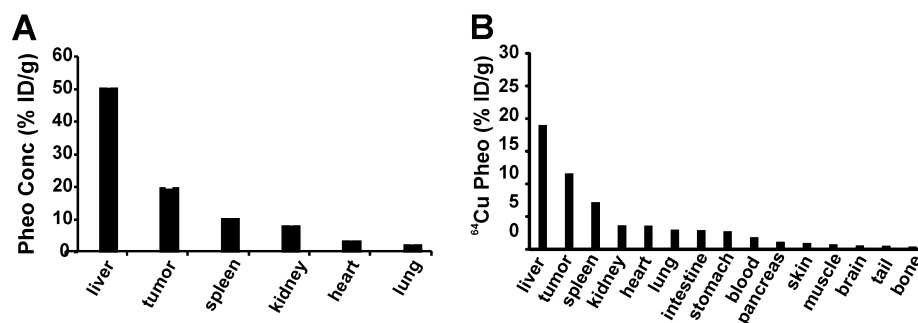


**Figure 7.** Biodistribution of ss-Pheo and  $^{64}\text{Cu}$ -labeled ss-Pheo (500  $\mu\text{g}$  Pheo) 24 h after intravenous administration in mice bearing orthotopic 4T1 tumors. (A) Pheo concentration in tumor and different organs as assess by fluorometric analysis of tissue homogenates. (B)  $^{64}\text{Cu}$ -labeled ss-Pheo (%ID/g) in tumor and different components of the body including cells, tissues, and organs. Data shows mean  $\pm$  standard deviation for  $n = 3$  mice.

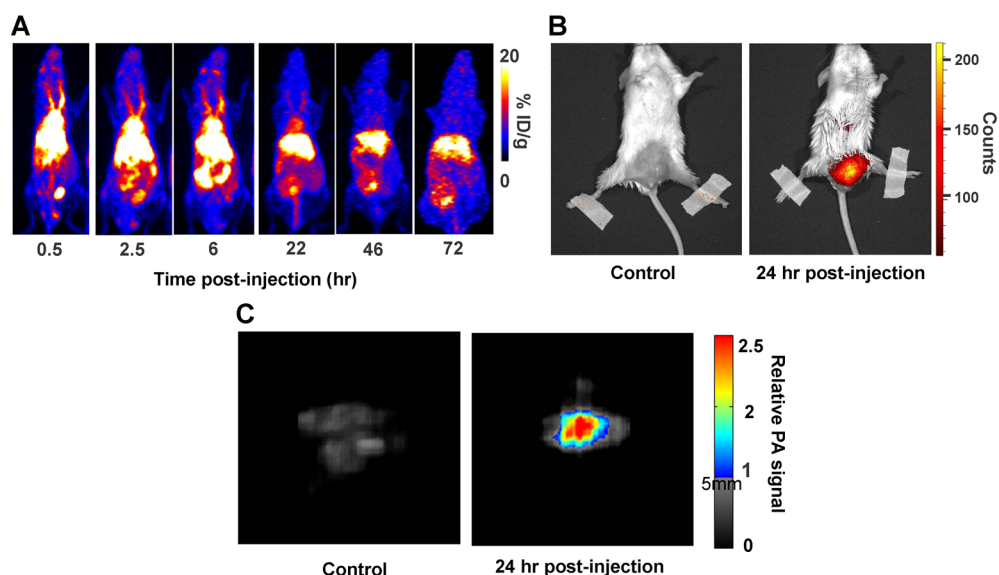


**Figure 8.** Trimodal imaging of ss-Pheo in vivo in mice bearing orthotopic 4T1 tumors. ss-Pheo ( $500 \mu\text{g}$ ) was injected intravenously per mouse. (A)  $^{64}\text{Cu}$ -labeled ss-Pheo PET scan at indicated time points. The tumor location is indicated by the white circle. (B) NIR fluorescence imaging in tumor-bearing mice either injected with ss-Pheo or untreated. (C) PAT imaging with control and treated mice. Representative images for  $n = 3$  mice per group.

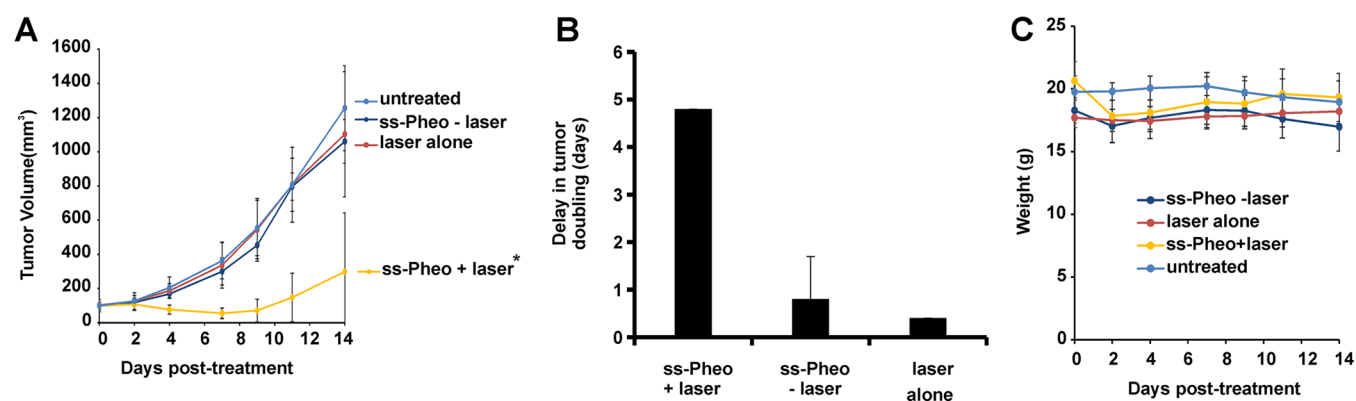


**Figure 9.** Tumor growth inhibition by ss-Pheo via PDT. Mice were intravenously administered  $500 \mu\text{g}$  of ss-Pheo and 24 h later were treated with  $300 \text{ J}/\text{cm}^2$  ( $150 \text{ mW}/\text{cm}^2$  fluence rate) with a  $665 \text{ nm}$  laser diode. (A) Tumor volume for mice bearing a 4T1 tumor following indicated treatments. The asterisk shows there was a significant difference between ss-Pheo+laser compared to other groups based on one-way ANOVA ( $p < 0.5$ ). (B) Tumor doubling delay was found for each treatment condition including Pheo alone, laser alone, and Pheo+laser. (C) Body weight in treated groups. Data show mean  $\pm$  standard deviation for  $n = 5$  mice per group.

Pheo contrast signal originating in the tumor. In the case of fluorescence imaging, the technique images superficial contrast so that the signal in the deeper liver may be obscured. Furthermore, the abdominal hair of the mice may have interfered with liver detection. In the case of photoacoustic imaging, we were specifically focusing the transducer on the tumor, so that signal in the liver would not be detected.

Given the favorable tumor accumulation, ss-Pheo was next assessed for photodynamic therapy. Following intravenous administration of  $500 \mu\text{g}$  of ss-Pheo, orthotopic 4T1 tumors were treated with  $300 \text{ J}/\text{cm}^2$  of  $665 \text{ nm}$  light using a laser diode (33 min of laser treatment with a  $150 \text{ mW cm}^{-2}$  fluence rate). Under these irradiation conditions, a mild tumor temperature rise occurred over the first 3 min, but stabilized thereafter with minimal tumor heating with a tumor surface temperature that did not surpass  $40 \text{ }^\circ\text{C}$  or rise more than  $5 \text{ }^\circ\text{C}$  overall (Figure S9). As shown in Figure 9A, this treatment was able to significantly delay tumor growth compared to ss-Pheo

treatment without a laser, and compared to laser treatment alone. Although the tumor growth inhibition delay was apparent, tumors started to grow back after approximately 1–2 weeks. To improve these results, it might be possible to use repeated PDT treatments in the future. The trend is consistent with the tumor doubling time, which shows an increase in delay tumor doubling time with ss-Pheo and laser treatment (Figure 9B). There was some short-term weight loss observed in the PDT-treated group; however, this was short-lived and mice fully recovered (Figure 9C). Further studies are required to characterize the toxicity and clearance of ss-Pheo. However, we note that Pheo is demetallated Chlr, which is consumed in human diets in abundance. The absorption and metabolism of Chlr have been studied previously.<sup>62,63</sup>

## CONCLUSION

Surfactant-stripped micelles represent a relatively new delivery vehicle with a high cargo to excipient ratio. Compared to two

other high-density porphyrin nanoparticles, ss-Pheo exhibited advantageous properties for optical imaging and photodynamic therapy. ss-Pheo was used for trimodal imaging with PET, PAT, and fluorescence imaging in vivo in a murine mammary tumor model. ss-Pheo had long circulation in mice and favorable tumor accumulation. ss-Pheo could be used as a photosensitizer. Further exploration of ss-Pheo for imaging and PDT applications is warranted.

## ■ ASSOCIATED CONTENT

### ● Supporting Information

The Supporting Information is available free of charge on the ACS Publications website at DOI: 10.1021/acsabm.8b00703.

Micelle size distribution; electron microscopy; fluorescence emission spectra in water and methanol; photo-thermal response; photobleaching; emission spectra in chloroform and surfactant; chelation stability of  $^{64}\text{Cu}$  in ss-Pheo; PET imaging biodistribution kinetics; tumor temperature during PDT (PDF)

## ■ AUTHOR INFORMATION

### Corresponding Author

\*E-mail: jflovel@buffalo.edu.

### ORCID

Weibo Cai: 0000-0003-4641-0833

Jonathan F. Lovell: 0000-0002-9052-884X

### Notes

The authors declare no competing financial interest.

## ■ ACKNOWLEDGMENTS

This work was supported by the National Institutes of Health (R01EB017270, DP5OD017898, R01CA169365, and P30CA014520) and the National Science Foundation (1555220).

## ■ REFERENCES

- (1) Lovell, J. F.; Liu, T. W. B.; Chen, J.; Zheng, G. Activatable Photosensitizers for Imaging and Therapy. *Chem. Rev.* **2010**, *110* (5), 2839–2857.
- (2) Agostinis, P.; Berg, K.; Cengel, K. A.; Foster, T. H.; Girotti, A. W.; Gollnick, S. O.; Hahn, S. M.; Hamblin, M. R.; Juzeniene, A.; Kessel, D.; Korbelik, M.; Moan, J.; Mroz, P.; Nowis, D.; Piette, J.; Wilson, B. C.; Golab, J. Photodynamic Therapy of Cancer: An Update. *CA. Ca-Cancer J. Clin.* **2011**, *61* (4), 250–281.
- (3) Kessel, D. Photodynamic Therapy: From the Beginning. *Photodiagn. Photodyn. Ther.* **2004**, *1* (1), 3–7.
- (4) Robertson, C. A.; Evans, D. H.; Abrahamse, H. Photodynamic Therapy (PDT): A Short Review on Cellular Mechanisms and Cancer Research Applications for PDT. *J. Photochem. Photobiol., B* **2009**, *96* (1), 1–8.
- (5) Berg, K.; Selbo, P. K.; Weyergang, A.; Dietze, A.; Prasmickaite, L.; Bonsted, A.; Engesaeter, B. Ø.; Angell-Petersen, E.; Warloe, T.; Frandsen, N.; Høgset, A. Porphyrin-Related Photosensitizers for Cancer Imaging and Therapeutic Applications. *J. Microsc.* **2005**, *218* (2), 133–147.
- (6) Celli, J. P.; Spring, B. Q.; Rizvi, I.; Evans, C. L.; Samkoe, K. S.; Verma, S.; Pogue, B. W.; Hasan, T. Imaging and Photodynamic Therapy: Mechanisms, Monitoring, and Optimization. *Chem. Rev.* **2010**, *110* (5), 2795–2838.
- (7) Yang, V. X. D.; Muller, P. J.; Herman, P.; Wilson, B. C. A Multispectral Fluorescence Imaging System: Design and Initial Clinical Tests in Intra-Operative Photofrin-Photodynamic Therapy of Brain Tumors. *Lasers Surg. Med.* **2003**, *32* (3), 224–232.
- (8) Wilson, B. C.; Patterson, M. S.; Lilge, L. Implicit and Explicit Dosimetry in Photodynamic Therapy: A New Paradigm. *Lasers Med. Sci.* **1997**, *12* (3), 182–199.
- (9) Pandey, S. K.; Gryshuk, A. L.; Sajjad, M.; Zheng, X.; Chen, Y.; Abouzeid, M. M.; Morgan, J.; Charamisinau, I.; Nabi, H. A.; Oseroff, A.; Pandey, R. K. Multimodality Agents for Tumor Imaging (PET, Fluorescence) and Photodynamic Therapy. A Possible “See and Treat” Approach. *J. Med. Chem.* **2005**, *48* (20), 6286–6295.
- (10) Li, G.; Slansky, A.; Dobhal, M. P.; Goswami, L. N.; Graham, A.; Chen, Y.; Kanter, P.; Alberico, R. A.; Spornyak, J.; Morgan, J.; Mazurchuk, R.; Oseroff, A.; Grossman, Z.; Pandey, R. K. Chlorophyll-a Analogues Conjugated with Aminobenzyl-DTPA as Potential Bifunctional Agents for Magnetic Resonance Imaging and Photodynamic Therapy. *Bioconjugate Chem.* **2005**, *16* (1), 32–42.
- (11) Luo, J.; Chen, L.-F.; Hu, P.; Chen, Z.-N. Tetranuclear Gadolinium(III) Porphyrin Complex as a Theranostic Agent for Multimodal Imaging and Photodynamic Therapy. *Inorg. Chem.* **2014**, *53* (8), 4184–4191.
- (12) Huang, H.; Lovell, J. F. Advanced Functional Nanomaterials for Theranostics. *Adv. Funct. Mater.* **2017**, *27* (2), 1603524.
- (13) Lim, E.-K.; Kim, T.; Paik, S.; Haam, S.; Huh, Y.-M.; Lee, K. Nanomaterials for Theranostics: Recent Advances and Future Challenges. *Chem. Rev.* **2015**, *115* (1), 327–394.
- (14) Bhaumik, J.; Mittal, A. K.; Banerjee, A.; Chisti, Y.; Banerjee, U. C. Applications of Phototheranostic Nanoagents in Photodynamic Therapy. *Nano Res.* **2015**, *8* (5), 1373–1394.
- (15) Bechet, D.; Couleaud, P.; Frochot, C.; Viriot, M.-L.; Guillemin, F.; Barberi-Heyob, M. Nanoparticles as Vehicles for Delivery of Photodynamic Therapy Agents. *Trends Biotechnol.* **2008**, *26* (11), 612–621.
- (16) Huang, P.; Lin, J.; Wang, X.; Wang, Z.; Zhang, C.; He, M.; Wang, K.; Chen, F.; Li, Z.; Shen, G.; Cui, D.; Chen, X. Light-Triggered Theranostics Based on Photosensitizer-Conjugated Carbon Dots for Simultaneous Enhanced-Fluorescence Imaging and Photodynamic Therapy. *Adv. Mater.* **2012**, *24* (37), 5104–5110.
- (17) Park, Y. I.; Kim, H. M.; Kim, J. H.; Moon, K. C.; Yoo, B.; Lee, K. T.; Lee, N.; Choi, Y.; Park, W.; Ling, D.; Na, K.; Moon, W. K.; Choi, S. H.; Park, H. S.; Yoon, S.-Y.; Suh, Y. D.; Lee, S. H.; Hyeon, T. Theranostic Probe Based on Lanthanide-Doped Nanoparticles for Simultaneous In Vivo Dual-Modal Imaging and Photodynamic Therapy. *Adv. Mater.* **2012**, *24* (42), 5755–5761.
- (18) Liu, K.; Liu, X.; Zeng, Q.; Zhang, Y.; Tu, L.; Liu, T.; Kong, X.; Wang, Y.; Cao, F.; Lambrechts, S. A. G.; Aalders, M. C. G.; Zhang, H. Covalently Assembled NIR Nanoplatform for Simultaneous Fluorescence Imaging and Photodynamic Therapy of Cancer Cells. *ACS Nano* **2012**, *6* (5), 4054–4062.
- (19) Shen, J.; Zhao, L.; Han, G. Lanthanide-Doped Upconverting Luminescent Nanoparticle Platforms for Optical Imaging-Guided Drug Delivery and Therapy. *Adv. Drug Delivery Rev.* **2013**, *65* (5), 744–755.
- (20) Liu, Y.; Meng, X.; Bu, W. Upconversion-Based Photodynamic Cancer Therapy. *Coord. Chem. Rev.* **2019**, *379*, 82.
- (21) Liu, Y.; Zhang, J.; Zuo, C.; Zhang, Z.; Ni, D.; Zhang, C.; Wang, J.; Zhang, H.; Yao, Z.; Bu, W. Upconversion Nano-Photosensitizer Targeting into Mitochondria for Cancer Apoptosis Induction and Cyt c Fluorescence Monitoring. *Nano Res.* **2016**, *9* (11), 3257–3266.
- (22) Wang, Y.; Wang, H.; Liu, D.; Song, S.; Wang, X.; Zhang, H. Graphene Oxide Covalently Grafted Upconversion Nanoparticles for Combined NIR Mediated Imaging and Photothermal/Photodynamic Cancer Therapy. *Biomaterials* **2013**, *34* (31), 7715–7724.
- (23) Rong, P.; Yang, K.; Srivastan, A.; Kiesewetter, D. O.; Yue, X.; Wang, F.; Nie, L.; Bhirde, A.; Wang, Z.; Liu, Z.; Niu, G.; Wang, W.; Chen, X. Photosensitizer Loaded Nano-Graphene for Multimodality Imaging Guided Tumor Photodynamic Therapy. *Theranostics* **2014**, *4* (3), 229–239.
- (24) Lin, J.; Wang, S.; Huang, P.; Wang, Z.; Chen, S.; Niu, G.; Li, W.; He, J.; Cui, D.; Lu, G.; Chen, X.; Nie, Z. Photosensitizer-Loaded Gold Vesicles with Strong Plasmonic Coupling Effect for Imaging-

Guided Photothermal/Photodynamic Therapy. *ACS Nano* **2013**, *7* (6), 5320–5329.

(25) Srivatsan, A.; Jenkins, S. V.; Jeon, M.; Wu, Z.; Kim, C.; Chen, J.; Pandey, R. K. Gold Nanocage-Photosensitizer Conjugates for Dual-Modal Image-Guided Enhanced Photodynamic Therapy. *Theranostics* **2014**, *4* (2), 163–174.

(26) Liu, G.; Ma, J.; Li, Y.; Li, Q.; Tan, C.; Song, H.; Cai, S.; Chen, D.; Hou, Z.; Chen, Q.; Zhu, X. Core-Interlayer-Shell Fe<sub>3</sub>O<sub>4</sub>@mSiO<sub>2</sub>@lipid-PEG-Methotrexate Nanoparticle for Multimodal Imaging and Multistage Targeted Chemo-Photodynamic Therapy. *Int. J. Pharm.* **2017**, *521* (1), 19–32.

(27) Fan, W.; Shen, B.; Bu, W.; Chen, F.; He, Q.; Zhao, K.; Zhang, S.; Zhou, L.; Peng, W.; Xiao, Q.; Ni, D.; Liu, J.; Shi, J. A Smart Upconversion-Based Mesoporous Silica Nanotheranostic System for Synergetic Chemo-/Radio-/Photodynamic Therapy and Simultaneous MR/UCL Imaging. *Biomaterials* **2014**, *35* (32), 8992–9002.

(28) Gong, H.; Dong, Z.; Liu, Y.; Yin, S.; Cheng, L.; Xi, W.; Xiang, J.; Liu, K.; Li, Y.; Liu, Z. Engineering of Multifunctional Nanomicelles for Combined Photothermal and Photodynamic Therapy Under the Guidance of Multimodal Imaging. *Adv. Funct. Mater.* **2014**, *24* (41), 6492–6502.

(29) Li, Z.; Zhang, Y.; Huang, L.; Yang, Y.; Zhao, Y.; El-Banna, G.; Han, G. Nanoscale “Fluorescent Stone”: Luminescent Calcium Fluoride Nanoparticles as Theranostic Platforms. *Theranostics* **2016**, *6* (13), 2380–2393.

(30) Hu, D.; Sheng, Z.; Gao, G.; Siu, F.; Liu, C.; Wan, Q.; Gong, P.; Zheng, H.; Ma, Y.; Cai, L. Activatable Albumin-Photosensitizer Nanoassemblies for Triple-Modal Imaging and Thermal-Modulated Photodynamic Therapy of Cancer. *Biomaterials* **2016**, *93*, 10–19.

(31) Lyu, Y.; Zeng, J.; Jiang, Y.; Zhen, X.; Wang, T.; Qiu, S.; Lou, X.; Gao, M.; Pu, K. Enhancing Both Biodegradability and Efficacy of Semiconducting Polymer Nanoparticles for Photoacoustic Imaging and Photothermal Therapy. *ACS Nano* **2018**, *12* (2), 1801–1810.

(32) Jiang, Y.; Cui, D.; Fang, Y.; Zhen, X.; Upputuri, P. K.; Pramanik, M.; Ding, D.; Pu, K. Amphiphilic Semiconducting Polymer as Multifunctional Nanocarrier for Fluorescence/Photoacoustic Imaging Guided Chemo-Photothermal Therapy. *Biomaterials* **2017**, *145*, 168–177.

(33) Miao, Q.; Xie, C.; Zhen, X.; Lyu, Y.; Duan, H.; Liu, X.; Jokerst, J. V.; Pu, K. Molecular Afterglow Imaging with Bright, Biodegradable Polymer Nanoparticles. *Nat. Biotechnol.* **2017**, *35* (11), 1102–1110.

(34) Jiang, Y.; Pu, K. Multimodal Biophotonics of Semiconducting Polymer Nanoparticles. *Acc. Chem. Res.* **2018**, *51* (8), 1840–1849.

(35) Miao, Q.; Pu, K. Organic Semiconducting Agents for Deep-Tissue Molecular Imaging: Second Near-Infrared Fluorescence, Self-Luminescence, and Photoacoustics. *Adv. Mater.* **2018**, *30* (49), 1801778.

(36) Liu, J.; Zheng, X.; Yan, L.; Zhou, L.; Tian, G.; Yin, W.; Wang, L.; Liu, Y.; Hu, Z.; Gu, Z.; Chen, C.; Zhao, Y. Bismuth Sulfide Nanorods as a Precision Nanomedicine for in Vivo Multimodal Imaging-Guided Photothermal Therapy of Tumor. *ACS Nano* **2015**, *9* (1), 696–707.

(37) Wen, L.; Chen, L.; Zheng, S.; Zeng, J.; Duan, G.; Wang, Y.; Wang, G.; Chai, Z.; Li, Z.; Gao, M. Ultrasmall Biocompatible WO<sub>3</sub>-x Nanodots for Multi-Modality Imaging and Combined Therapy of Cancers. *Adv. Mater.* **2016**, *28* (25), 5072–5079.

(38) Huang, L.; Li, Z.; Zhao, Y.; Yang, J.; Yang, Y.; Pendharkar, A. I.; Zhang, Y.; Kelmar, S.; Chen, L.; Wu, W.; Zhao, J.; Han, G. Enhancing Photodynamic Therapy through Resonance Energy Transfer Constructed Near-Infrared Photosensitized Nanoparticles. *Adv. Mater.* **2017**, *29* (28), 1604789.

(39) Zhu, H.; Fang, Y.; Miao, Q.; Qi, X.; Ding, D.; Chen, P.; Pu, K. Regulating Near-Infrared Photodynamic Properties of Semiconducting Polymer Nanotheranostics for Optimized Cancer Therapy. *ACS Nano* **2017**, *11* (9), 8998–9009.

(40) Zhu, H.; Li, J.; Qi, X.; Chen, P.; Pu, K. Oxygenic Hybrid Semiconducting Nanoparticles for Enhanced Photodynamic Therapy. *Nano Lett.* **2018**, *18* (1), 586–594.

(41) Huang, L.; Li, Z.; Zhao, Y.; Zhang, Y.; Wu, S.; Zhao, J.; Han, G. Ultralow-Power Near Infrared Lamp Light Operable Targeted Organic Nanoparticle Photodynamic Therapy. *J. Am. Chem. Soc.* **2016**, *138* (44), 14586–14591.

(42) Chen, L.; Chen, J.; Qiu, S.; Wen, L.; Wu, Y.; Hou, Y.; Wang, Y.; Zeng, J.; Feng, Y.; Li, Z.; Shan, H.; Gao, M. Biodegradable Nanoagents with Short Biological Half-Life for SPECT/PAI/MRI Multimodality Imaging and PTT Therapy of Tumors. *Small* **2018**, *14* (4), 1702700.

(43) Zeng, J.; Cheng, M.; Wang, Y.; Wen, L.; Chen, L.; Li, Z.; Wu, Y.; Gao, M.; Chai, Z. PH-Responsive Fe(III)-Gallic Acid Nanoparticles for In Vivo Photoacoustic-Imaging-Guided Photothermal Therapy. *Adv. Healthcare Mater.* **2016**, *5* (7), 772–780.

(44) Jiang, X.; Zhang, S.; Ren, F.; Chen, L.; Zeng, J.; Zhu, M.; Cheng, Z.; Gao, M.; Li, Z. Ultrasmall Magnetic CuFeSe<sub>2</sub> Ternary Nanocrystals for Multimodal Imaging Guided Photothermal Therapy of Cancer. *ACS Nano* **2017**, *11* (6), 5633–5645.

(45) Kim, C.; Favazza, C.; Wang, L. V. In Vivo Photoacoustic Tomography of Chemicals: High-Resolution Functional and Molecular Optical Imaging at New Depths. *Chem. Rev.* **2010**, *110* (5), 2756–2782.

(46) Ho, C. J. H.; Balasundaram, G.; Driessen, W.; McLaren, R.; Wong, C. L.; Dinish, U. S.; Attia, A. B. E.; Ntziachristos, V.; Olivo, M. Multifunctional Photosensitizer-Based Contrast Agents for Photoacoustic Imaging. *Sci. Rep.* **2015**, *4*, 5342.

(47) Bonnett, R. Photosensitizers of the Porphyrin and Phthalocyanine Series for Photodynamic Therapy. *Chem. Soc. Rev.* **1995**, *24* (1), 19–33.

(48) Zhang, Y.; Lovell, J. F. Porphyrins as Theranostic Agents from Prehistoric to Modern Times. *Theranostics* **2012**, *2* (9), 905–915.

(49) Huang, H.; Song, W.; Rieffel, J.; Lovell, J. F. Emerging Applications of Porphyrins in Photomedicine. *Front. Phys.* **2015**, *3*, 23.

(50) Zhou, Y.; Liang, X.; Dai, Z. Porphyrin-Loaded Nanoparticles for Cancer Theranostics. *Nanoscale* **2016**, *8* (25), 12394–12405.

(51) Huynh, E.; Zheng, G. Porphyrins Nanotechnology: A Paradigm Shift in Lipid-Based Supramolecular Structures. *Nano Today* **2014**, *9* (2), 212–222.

(52) Lovell, J. F.; Jin, C. S.; Huynh, E.; Jin, H.; Kim, C.; Rubinstein, J. L.; Chan, W. C. W.; Cao, W.; Wang, L. V.; Zheng, G. Porphyrinsome Nanovesicles Generated by Porphyrin Bilayers for Use as Multimodal Biophotonic Contrast Agents. *Nat. Mater.* **2011**, *10* (4), 324–332.

(53) Zhang, Y.; Jeon, M.; Rich, L. J.; Hong, H.; Geng, J.; Zhang, Y.; Shi, S.; Barnhart, T. E.; Alexandridis, P.; Huizinga, J. D.; Seshadri, M.; Cai, W.; Kim, C.; Lovell, J. F. Non-Invasive Multimodal Functional Imaging of the Intestine with Frozen Micellar Naphthalocyanines. *Nat. Nanotechnol.* **2014**, *9* (8), 631–638.

(54) Zhang, Y.; Song, W.; Geng, J.; Chitgupi, U.; Unsal, H.; Federizon, J.; Rzaev, J.; Sukumaran, D. K.; Alexandridis, P.; Lovell, J. F. Therapeutic Surfactant-Stripped Frozen Micelles. *Nat. Commun.* **2016**, *7*, 11649.

(55) Zhang, Y.; Wang, D.; Goel, S.; Sun, B.; Chitgupi, U.; Geng, J.; Sun, H.; Barnhart, T. E.; Cai, W.; Xia, J.; Lovell, J. F. Surfactant-Stripped Frozen Pheophytin Micelles for Multimodal Gut Imaging. *Adv. Mater.* **2016**, *28* (38), 8524–8530.

(56) Xu, M.; Wang, L. V. Universal Back-Projection Algorithm for Photoacoustic Computed Tomography. *Phys. Rev. E Stat. Nonlin. Soft Matter Phys.* **2005**, *71*, 016706.

(57) Forster, L. S.; Livingston, R. The Absolute Quantum Yields of the Fluorescence of Chlorophyll Solutions. *J. Chem. Phys.* **1952**, *20* (8), 1315–1320.

(58) Lovell, J. F.; Chen, J.; Jarvi, M. T.; Cao, W.-G.; Allen, A. D.; Liu, Y.; Tidwell, T. T.; Wilson, B. C.; Zheng, G. FRET Quenching of Photosensitizer Singlet Oxygen Generation. *J. Phys. Chem. B* **2009**, *113* (10), 3203–3211.

(59) Flors, C.; Fryer, M. J.; Waring, J.; Reeder, B.; Bechtold, U.; Mullineaux, P. M.; Nonell, S.; Wilson, M. T.; Baker, N. R. Imaging the Production of Singlet Oxygen in Vivo Using a New Fluorescent Sensor, Singlet Oxygen Sensor Green. *J. Exp. Bot.* **2006**, *57* (8), 1725–1734.

(60) Jokerst, J. V.; Lobovkina, T.; Zare, R. N.; Gambhir, S. S. Nanoparticle PEGylation for Imaging and Therapy. *Nanomedicine* **2011**, *6* (4), 715–728.

(61) Nie, S. Understanding and Overcoming Major Barriers in Cancer Nanomedicine. *Nanomedicine* **2010**, *5* (4), 523–528.

(62) Ferruzzi, M. G.; Blakeslee, J. Digestion, Absorption, and Cancer Preventative Activity of Dietary Chlorophyll Derivatives. *Nutr. Res. (N. Y., NY, U. S.)* **2007**, *27* (1), 1–12.

(63) Ma, L.; Dolphin, D. The Metabolites of Dietary Chlorophylls. *Phytochemistry* **1999**, *50* (2), 195–202.